

This is a preprint of a manuscript accepted and published in Quaternary Science Reviews.
The published version of this manuscript can be found at <https://doi.org/10.1016/j.gca.2022.11.001>

1 **Weak precipitation $\delta^2\text{H}$ response to large Holocene hydroclimate changes**
2 **in eastern North America**

3 Ioana C. Stefanescu^{1*}, Bryan N. Shuman¹, Laurie D. Grigg², Adriana Bailey³, Vania Stefanova⁴,
4 W. Wyatt Oswald⁵

5 ^{1*}Department of Geology and Geophysics, University of Wyoming

6 ²Department of Earth and Environmental Sciences, Norwich University

7 ³National Center for Atmospheric Research, Boulder, Colorado

8 ⁴Continental Scientific Drilling Facility and Limnological Research Center, University of
9 Minnesota

10 ⁵Marlboro Institute for Liberal Arts and Interdisciplinary Studies, Emerson College, Boston, MA

11 Corresponding author: Ioana C. Stefanescu

12 Address: 1000 E University Ave, Science Initiative Room 4234, Laramie, Wyoming, 82071,
13 United States of America

14 E-mail: *istefane@uwyo.edu*

15 **ABSTRACT**

16 In eastern North America, annual precipitation increased by >40% over the Holocene,
17 largely in response to melting of the Laurentide Ice Sheet. The change substantially raised lake
18 levels and transformed conifer-dominated ecosystems into mesic deciduous forests. $\delta^2\text{H}$ values
19 of terrestrially derived leaf-wax *n*-alkanes can facilitate diagnoses of the climate dynamics
20 involved by reconstructing $\delta^2\text{H}$ values of mean annual precipitation ($\delta^2\text{H}_{\text{MAP}}$). However,
21 competing influences on $\delta^2\text{H}_{\text{MAP}}$ values in the mid-latitudes, such as changes in moisture sources
22 and in the seasonal distribution of precipitation, can generate confounding effects. To test
23 $\delta^2\text{H}_{\text{MAP}}$ sensitivity to potential changes associated with the final Holocene phases of deglaciation
24 in eastern North America, we used 14 fossil-pollen records to reconstruct monthly precipitation
25 changes and to model $\delta^2\text{H}_{\text{MAP}}$ values during the Holocene. The pollen-inferred precipitation
26 increased by 100-200 mm during both cold and warm seasons, but modelled $\delta^2\text{H}_{\text{MAP}}$ values
27 changed by only ~10‰, because isotopically-heavy summer precipitation increased by nearly as
28 much as the cold-season isotopically-light winter precipitation. Three new leaf wax *n*-C₂₉-alkane
29 ($\delta^2\text{H}_{\text{C29}}$) records spanning the Holocene from Vermont, Pennsylvania, and Massachusetts closely
30 follow modeled $\delta^2\text{H}_{\text{MAP}}$ trends and confirm only a small decline in $\delta^2\text{H}_{\text{MAP}}$ values over the
31 Holocene. Because the shifts in precipitation seasonality accurately predict the *n*-alkane records,
32 changes in moisture sources or pathways appear to play only a minor role in the regional $\delta^2\text{H}_{\text{MAP}}$
33 history despite the effects of deglaciation on atmospheric circulation. Soil evaporation also did
34 not significantly alter $\delta^2\text{H}_{\text{C29}}$ values from the values predicted using the pollen-derived
35 reconstructions. The results affirm that $\delta^2\text{H}_{\text{C29}}$ values faithfully detected anticipated isotopic

36 changes in $\delta^2\text{H}_{\text{MAP}}$ values, but that important paleoclimate events may not always yield strong
37 changes in $\delta^2\text{H}_{\text{MAP}}$ values.

38 1. INTRODUCTION

39 Due to the geographic position of the northeastern United States, the region has
40 experienced major climate changes over the Holocene (~11.7 kyrs to present) driven by the
41 retreat of the Laurentide Ice Sheet (LIS), orbitally-forced insolation changes, and the dynamics
42 of the adjacent North Atlantic Ocean (Webb et al., 1993; Shuman and Marsicek 2016; Shuman
43 and Plank, 2011; Shuman et al., 2019). An Early Holocene (~8 ka) shift from ice-sheet-
44 dominated climate trends to those driven by seasonal insolation changes triggered a >40%
45 increase in regional precipitation and a major shift from conifer to deciduous forests (Shuman et
46 al., 2002; Shuman et al., 2009; Oswald et al., 2018; Shuman et al., 2019). The accelerated
47 decline of the LIS around ca. 8.2 ka likely had implications for regional atmospheric circulation,
48 the frequency of different types of precipitation events (e.g., ‘nor’easter’ storms, tropical
49 cyclones), and the seasonality of precipitation, while summer insolation anomalies likely
50 influenced evaporation rates (Shuman and Donnelly, 2006). Stable isotope records may provide
51 insight into how such processes contributed to the large hydroclimate and ecosystem changes
52 (e.g., Kirby et al., 2002; Shuman et al., 200; ,Hou et al., 2007; Mandl et al. 2016; Gao et al.,
53 2017). However, amid these large Holocene climate shifts, *n*-C₂₉ $\delta^2\text{H}$ records ($\delta^2\text{H}_{\text{C29}}$) from the
54 northeastern U.S., such as from the Adirondack Mountains (New York), suggest a limited range
55 of variation in the $\delta^2\text{H}$ composition of precipitation over the Holocene (~10‰; Schartman et al.,
56 2020). This pattern extends further west into Wisconsin where the $\delta^2\text{H}$ record from Lake Geneva
57 also shows little variability over the Holocene (Puleo et al., 2020).

58 The $\delta^2\text{H}_{\text{C}_{29}}$ records pose a fascinating paradox because a lack of $\delta^2\text{H}$ change during large-
59 scale regional transformation defies expectations about both the climate changes involved and
60 the sensitivity of $\delta^2\text{H}_{\text{C}_{29}}$ records to mid-latitude hydroclimatology. Here, we explore the
61 conundrum. In doing so, we use a multi-proxy context and the dynamic hydroclimate history of
62 the northeastern U.S. as an opportunity to evaluate how networks of $\delta^2\text{H}_{\text{C}_{29}}$ records represent
63 hydrologic changes in the mid-latitudes.

64 Leaf wax *n*-alkanes preserved in sedimentary archives are increasingly being used here
65 and elsewhere to reconstruct past moisture trends (Scheffuß et al., 2005; Tierney et al., 2010;
66 Rach et al., 2014; Basu et al., 2019; Cao et al., 2020; Puleo et al., 2020; Schartman et al.,
67 2020; Toney et al., 2020). *n*-Alkanes are odd-numbered hydrocarbons synthesized by both
68 terrestrial and aquatic plants using environmental waters that ultimately originate from
69 precipitation (Sachse et al., 2012). Therefore, $\delta^2\text{H}_{\text{wax}}$ reflects the $\delta^2\text{H}$ composition of
70 precipitation. Strong relationships at both regional and global scales between the $\delta^2\text{H}$ values of
71 mean annual precipitation ($\delta^2\text{H}_{\text{MAP}}$) and those of terrestrial plants leaf-waxes (i.e., *n*-C₂₉-alkane)
72 make these compounds a suitable proxy for inferring the $\delta^2\text{H}$ values of past precipitation (Sachse
73 et al., 2004; Sachse et al., 2006; Garcin et al., 2012; Sachse et al., 2012; Tipple et al.,
74 2013; Freimuth et al., 2017; McFarlin et al., 2019; Stefanescu et al., 2023). As the $\delta^2\text{H}$ values of
75 precipitation at a given location are strongly controlled by atmospheric circulation and rainout
76 processes (Craig 1961; Gat 1996; Dansgaard 1964), the $\delta^2\text{H}$ values of terrestrial leaf-waxes
77 provide an opportunity to reconstruct the drivers behind past climate changes such as shifts in
78 atmospheric circulation and moisture sources.

79 Here, we expand the leaf wax *n*-C₂₉ $\delta^2\text{H}$ datasets from the northeastern U.S. region to
80 include new coastal, inland, and northern records and compare the *n*-C₂₉-alkane-based

81 reconstructed $\delta^2\text{H}$ values of mean annual precipitation ($\delta^2\text{H}_{\text{MAP_C29}}$) to pollen-inferred
82 expectations of precipitation $\delta^2\text{H}$ change ($\delta^2\text{H}_{\text{MAP}}$). We first confirm that fossil pollen records
83 from across the region indicate major changes in moisture availability, consistent with previous
84 analyses of regional pollen data (Webb et al., 1993; Marsicek et al., 2013; Shuman et al., 2019)
85 and lake-level reconstructions (Shuman et al., 2001; Newby et al., 2011; 2014; Shuman et al.,
86 2019). Then, to understand potential outcomes in the $\delta^2\text{H}_{\text{MAP_C29}}$ records, we combine the pollen-
87 inferred precipitation history with modern $\delta^2\text{H}$ values in monthly precipitation to test the
88 sensitivity of $\delta^2\text{H}_{\text{MAP}}$ to the observed changes in precipitation seasonality alone (i.e., without
89 accounting for changes in sources, circulation, and other influences on monthly $\delta^2\text{H}$ values).
90 Finally, we compare the simulated $\delta^2\text{H}_{\text{MAP}}$ expectations with the three new $\delta^2\text{H}_{\text{MAP_C29}}$ records
91 from Vermont, Pennsylvania, and Massachusetts and assess both the temporal trends and spatial
92 isotopic patterns to evaluate the roles of three major factors: (1) changes in precipitation
93 seasonality, (2) changes in moisture sources and pathways, and (3) evaporative effects on soil
94 moisture. The results have implications for interpreting the sensitivity of $\delta^2\text{H}_{\text{MAP_C29}}$ to complex,
95 multi-dimensional hydroclimate changes and can help establish benchmark expectations for
96 isotope-enabled climate model simulations of the Early Holocene (i.e., a strong regional
97 precipitation change associated with a modest $\delta^2\text{H}_{\text{MAP}}$ change).

98 **2. MATERIALS AND METHODS**

99 **2.1. Study sites**

100 We present three new leaf-wax *n*-C₂₉-alkane records from Twin Ponds (Vermont),
101 Blanding Lake (Pennsylvania) and Crooked Pond (Massachusetts) (Figure 1, Table 1). Twin
102 Ponds fills two adjoining glacially-scoured basins within the limestone member of the Waits
103 River Formation in east-central Vermont and is surrounded by northern hardwood forest

104 dominated by a mix of angiosperm and gymnosperm tree species such as sugar maples (*Acer*
105 *saccharum*), American beech (*Fagus grandifolia*), and eastern hemlock (*Tsuga canadensis*)
106 (Grigg et al., 2021). Crooked Pond is a small kettle lake composed of two basins within sandy
107 outwash near coastal Massachusetts. Pines (*Pinus* spp.) and oak (*Quercus* spp.) dominate the
108 surrounding sand-plain vegetation (Shuman et al., 2001). The sandy soils limited vegetation
109 changes at Crooked Pond during the Holocene (Shuman et al., 2001). We use the near-by pollen
110 record from Deep-Taunton Pond (Oswald et al., 2018), located on adjacent glacial tills and
111 surrounded by oak-dominated deciduous forest, to represent the regional vegetation changes near
112 Crooked Pond. Blanding Lake occupies a basin in glacial till in a valley incised within the
113 Allegheny Plateau in northeastern Pennsylvania and is underlain by fluvial sandstones of the
114 Catskill Formation. The immediate watershed contains a plantation of white pine (*Pinus strobus*)
115 and mixed deciduous forest dominated by oak species (*Quercus* spp.) (Shuman and Burrell,
116 2017).

117 Sediment cores from Twin Ponds, Blanding Lake and Crooked Pond were collected using
118 a hand-driven piston corer with 70 mm polycarbonate tubes. The total sediment core lengths
119 were 4.83 m, 10.12 m and 6.13 m, respectively. The Twin Ponds sediment core was collected at
120 a shallow water depth of 0.79 m, in a carbonate bench adjacent to the shore, while the sediment
121 cores from Blanding Lake and Crooked Pond were collected from the deepest locations within
122 the lakes at water depths of 5.55 m and 4.25 m, respectively. An additional core was also
123 collected from 7.8 m of water at the center of Twin Ponds western basin. Age models for the
124 0.79 m depth sediment core from Twin Ponds, and for the sediment cores from Blanding Lake
125 and Crooked Pond were derived from radiocarbon dates (Figure 2, Table 2) calibrated to
126 calendar years using the bchron package with the IntCal20 calibration curve (Haslett and Parnell,

127 2008; Reimer et al., 2020). We also generated new chronologies for the $\delta^2\text{H}_{\text{MAP_C29}}$ records at
128 Heart and Moose lakes (Schartman et al., 2020) using IntCal20.

129 **2.2. n-Alkane extraction and instrumental analysis**

130 *n*-Alkanes were extracted from 2-8 grams freeze-dried sediment and analyzed for $\delta^2\text{H}$
131 values on a Thermo Scientific Trace GC coupled to a Thermo Delta V IRMS following the
132 methods of Stefanescu et al. (2023). All samples were run in duplicates. A standard *n*-alkane
133 mixture (mixture A7 from Arndt Schimmelmann, Indiana University) containing alkanes *n*-C₁₆
134 to *n*-C₃₀ was used to identify *n*-alkane compounds based on retention times, and to account for
135 instrument D/H offset. The average H_3^+ factor for all runs was 2.19 and ranged between 1.98 to
136 2.21 across all runs. All $\delta^2\text{H}$ measurements are reported in ‰ relative to the Vienna Standard
137 Ocean Water (VSMOW). Sample duplicate $\delta^2\text{H}$ measurements were averaged, and the average
138 standard deviation of duplicates was 2.4 ‰ across all runs.

139 The $\delta^2\text{H}_{\text{C29}}$ analysis at Twin Ponds was completed on the shallow carbonate core where
140 additional oxygen isotope analyses will also be possible for future comparison. To compare the
141 range of $\delta^2\text{H}_{\text{C29}}$ values between the two cores, we also analyzed $\delta^2\text{H}_{\text{C29}}$ values in four sediment
142 samples from the sediment core collected at a water depth of 7.8 m. From here on, we refer to the
143 sediment core collected near the shore at the water depth of 0.79 m as the “shallow water core”
144 and to the core collected from the lake center at a depth of 7.8 m as the “deep water core”.

145 We use *n*-C₂₉-alkane $\delta^2\text{H}$ values to infer $\delta^2\text{H}_{\text{MAP}}$ values by applying the North American
146 average apparent fractionation factor (ϵ_{app}) of -131‰ (Stefanescu et al., 2023). The inferred
147 Holocene $\delta^2\text{H}_{\text{MAP_C29}}$ values at each lake were calculated as follows:

$$148 \delta^2\text{H}_{\text{MAP_C29}}\text{‰} = 1000 \times \left[\frac{\delta^2\text{H}_{\text{C29}}\text{‰} + 1000}{-131\text{‰} + 1000} - 1 \right] \quad \text{Eq.1}$$

149 2.3. Pollen analysis and climate reconstructions

150 We present new fossil pollen records from Twin Ponds (VT) and Blanding Lake (PA)
151 (Figure 1, Table 1) as part of an effort to compare the inferred $\delta^2\text{H}_{\text{MAP_C29}}$ values to pollen-
152 inferred estimates of Holocene hydroclimate changes and their isotopic consequences. Sediment
153 samples from Twin Ponds (VT) and Blanding Lake (PA) were prepared for pollen analysis
154 following a standard procedure (Faegri and Iversen. 1975) and analyzed for fossil pollen and
155 spores. Pollen of aquatic plants, fern, mosses, and fungal spores were excluded from the pollen
156 sum. The results are presented as percentages, calculated relative to the sum of all terrestrial taxa
157 and simplified pollen diagrams for the two lakes include the major pollen types discussed in the
158 text (Figure 4). For regional comparison, an additional 12 fossil-pollen records were obtained
159 from the Neotoma Palaeoecological Database (Figure 1, Table 1) (Williams et al., 2018). This
160 network of detailed pollen records was used to examine the coherency between local and
161 regional pollen-based moisture reconstructions over the Holocene. We use detailed fossil pollen
162 records from 14 sites in the region (Figure 1, Table 1) including Twin Ponds (VT), Blanding
163 Lake (PA), and Heart Lake (NY) (Whitehead and Jackson, 1990). Chronologies for all pollen
164 records were updated using the bchron package with the IntCal20 calibration curve (Parnell et
165 al., 2008; Reimer et al., 2020).

166 We reconstructed monthly precipitation changes from the pollen data at the 14 sites
167 (Figure 1, Figure 5, Figure 6) using the modern analogue technique, which compares each fossil
168 pollen sample to their most analogous modern pollen samples (Overpeck et al., 1985). The
169 modern monthly precipitation rates associated with the modern pollen samples are assumed to
170 represent the paleoclimate conditions as has been done previously for this region (e.g., Marsicek
171 et al., 2013). The modern pollen samples were derived from sites in North America east of 95°W

172 and were compared to the fossil pollen samples using the squared-chord distance (SCD) metric
173 (Overpeck et al., 1985). The comparisons measure the differences in the relative abundances of
174 54 important regional pollen types (Marsicek et al., 2013). The five modern pollen samples with
175 the lowest SCDs were considered analogs for each fossil pollen sample. The modern mean
176 monthly precipitation from the location of each analog was obtained from Whitmore et al. (2005)
177 and then the values for the five analogs were averaged and assigned as the paleo-precipitation
178 values. While the approach is imperfect, it builds upon the ability of the modern analog
179 technique to reconstruct precipitation during all seasons (Williams and Shuman, 2008). Warm
180 and cold season precipitation totals (Figure 6) were calculated by summing the reconstructed
181 monthly precipitation for June-November and December-May, respectively, while the warm/cold
182 season precipitation ratio was calculated by dividing their sums.

183 **2.4. Modern and modeled $\delta^2\text{H}$ values of precipitation**

184 Modern monthly and mean annual precipitation (MAP) $\delta^2\text{H}$ values were obtained using
185 the Online Isotopes of Precipitation Calculator (OIPC) (Bowen, G. J., 2020) and are reported
186 relative to VSMOW (Figure 1, Figure 3A). Modern monthly and mean annual precipitation
187 inputs (mm) were obtained from the Parameter-Elevation Regressions on Independent Slopes
188 Model (PRISM) with a resolution of 800 m, from the Climate Group at Oregon State University
189 (Prism Climate Group, 2021; Figure 3B, Table 1). To test the accuracy of OIPC $\delta^2\text{H}$ values, we
190 compare OIPC monthly and annual $\delta^2\text{H}$ values to measured monthly precipitation and soil
191 moisture $\delta^2\text{H}$ values from the nearby site of Hubbard Brook, New Hampshire (Figure 1A,B;
192 Campbell and Greene, 2019).

193 As pollen-inferred precipitation changes suggest that modern precipitation in the region
194 generally exceeds the rates of the last 14 kyrs (Webb et al., 1993; Shuman et al., 2019), we

195 model the potential sensitivity of $\delta^2\text{H}_{\text{MAP}}$ to reduced seasonal precipitation rates. To do so, we
196 first computed percent decreases from modern precipitation values (in 10 % increments) for
197 warm-season (June-November) and cold-season (December-May) precipitation, respectively,
198 which we combined with modern monthly $\delta^2\text{H}$ values to calculate expected $\delta^2\text{H}_{\text{MAP}}$ values as in
199 Eq.2. The results estimate how the reduction in precipitation in either season today would alter
200 the total isotopic composition of annual precipitation ($\delta^2\text{H}_{\text{MAP}}$) by shifting the weighting of
201 isotopic inputs in favor of the other season:

$$202 \quad \text{Modeled } \delta^2\text{H}_{\text{MAP}} \text{‰} = \frac{\sum(P_{\text{month}}(\text{mm}) \times \delta^2\text{H}_{\text{month}} \text{‰})}{\text{MAP (mm)}} \quad \text{Eq.2}$$

203 where P_{month} represents the mean precipitation amount of each month from January to
204 December and where $\delta^2\text{H}_{\text{month}}$ equals a fixed value for each month at each site as determined by
205 OIPC.

206 We then compute expected $\delta^2\text{H}_{\text{MAP}}$ departures from modern OIPC $\delta^2\text{H}_{\text{MAP}}$ values using
207 Eq. 3:

$$208 \quad \Delta\delta^2\text{H}_{\text{MAP}} \text{‰} = \text{modern } \delta^2\text{H}_{\text{MAP}} \text{‰} - \text{modeled } \delta^2\text{H}_{\text{MAP}} \text{‰} \quad \text{Eq.3}$$

209 To examine the effect of the inferred changes in precipitation seasonality over the past 14
210 kyrs, we then repeated this modelling of $\delta^2\text{H}_{\text{MAP}}$ using Eq. 2 by combining the monthly
211 precipitation input (mm) reconstructed from the fossil pollen with the fixed modern monthly
212 precipitation $\delta^2\text{H}$ values from OIPC at each pollen site. The goal is to estimate the sensitivity of
213 $\delta^2\text{H}_{\text{MAP}}$ values to the reconstructed seasonal precipitation changes alone and then compare with
214 the measured $\delta^2\text{H}_{\text{MAP_C29}}$ values to diagnose attendant changes in vapor sources, circulation
215 pathways, precipitation mechanisms, or soil evaporation, which we assume would create
216 departures from modeled $\delta^2\text{H}_{\text{MAP}}$ values in the measured $\delta^2\text{H}_{\text{MAP_C29}}$ values.

217 3. RESULTS AND DISCUSSION

218 3.1. Modern precipitation $\delta^2\text{H}$ values in the northeastern U.S. and their sensitivity to 219 change

220 To test the accuracy of modeled isotopic values in monthly precipitation and the effects
221 of evaporation on soil moisture isotopic values across the region, we use the modern long-term
222 (2007-2010) isotopic measurements of monthly precipitation and soil moisture from Hubbard
223 Brook, NH (Figure 1; Campbell and Greene, 2019). Hubbard Brook is located at a similar
224 latitude and elevation as our sites in Vermont and New York, and has similar precipitation inputs
225 and associated $\delta^2\text{H}$ isotopic values (Table 1, Figure 1). Therefore, the long-term isotopic record
226 of modern precipitation and soil moisture from Hubbard Brook is representative of the region.
227 Modern monthly precipitation and soil water $\delta^2\text{H}$ values measured at Hubbard Brook (Figure 1B;
228 Campbell and Greene, 2019) show 40‰-60‰ seasonal variation and a 3‰ difference in $\delta^2\text{H}_{\text{MAP}}$
229 values, suggesting little evaporation effects on soil water $\delta^2\text{H}$ values. These findings indicate that
230 terrestrial leaf wax source water (i.e., soil moisture) should closely track the $\delta^2\text{H}$ composition of
231 MAP with minimal evaporation effects. Moreover, modeled monthly and annual $\delta^2\text{H}$ values at
232 Hubbard Brook (NH) parallel those of measured precipitation and are similar to those modeled at
233 Twin Ponds, VT (Figure 1B). Furthermore, modeled $\delta^2\text{H}$ values match those observed at
234 Hubbard Brook suggesting that OIPC (Bowen, 2020) is suitable for predicting modern monthly
235 and annual $\delta^2\text{H}$ values across the region.

236 Modern monthly precipitation $\delta^2\text{H}$ values (from OIPC) range from -132 to -11‰ across
237 the region (Figure 3A) with the most negative values observed at the inland sites from New
238 York, Vermont and Pennsylvania where the range in monthly $\delta^2\text{H}$ values is -132 to -21‰. A
239 smaller range in monthly $\delta^2\text{H}$ values of -90 to -11‰ is observed at the coastal sites of

240 Massachusetts. Modern monthly precipitation values (from PRISM) range from 50 to 140 mm
241 across the region (Figure 3B) and show distinctive seasonality patterns. The inland sites receive
242 more precipitation during the warm season while the coastal sites of Massachusetts receive more
243 even monthly precipitation totals with modest peaks during March-April and November-
244 December (purple shading, Figure 3B).

245 Estimating the change in $\delta^2\text{H}_{\text{MAP}}$ values using Eq. 2 and 3 reveals that a decrease in either
246 cold- or warm-season precipitation inputs would only have a moderate effect on $\delta^2\text{H}_{\text{MAP}}$ values
247 across the region (Figure 3C,D). For example, a 50% reduction in cold-season precipitation
248 would only increase $\delta^2\text{H}_{\text{MAP}}$ values by a maximum 10.6‰. Conversely, a 100% reduction would
249 only lead to a maximum increase of 23.4‰. Similarly, 50% and 100% reductions in warm-
250 season precipitation would only decrease $\delta^2\text{H}_{\text{MAP}}$ values by up to 8.1‰ and 27.6‰, respectively.
251 Furthermore, combined reductions in both cold- and warm-season precipitation inputs would
252 likely neutralize changes in $\delta^2\text{H}_{\text{MAP}}$ values across the region as an increase of ~10‰ driven by
253 halving winter precipitation could be offset by a decrease of ~8‰ resulting from a halving of
254 summer precipitation, yielding a net effect of only ~2‰.

255 Additionally, our model shows that decreases in cold- or warm-season precipitation
256 would produce greater changes in $\delta^2\text{H}_{\text{MAP}}$ values at the inland sites compared to the coastal sites
257 of Massachusetts (Figure 3C). For example, because cold-season precipitation $\delta^2\text{H}$ values at the
258 inland sites (mean of -91‰) are lower than at the coastal sites (mean of -63‰), a decrease in
259 cold-season precipitation would generate larger changes in $\delta^2\text{H}_{\text{MAP}}$ values at the inland sites.

260 **3.2. Pollen-inferred vegetation changes**

261 Pollen-inferred vegetation changes at Heart Lake (NY), Twin Ponds (VT), Blanding Lake
262 (PA), and Deep-Taunton Pond (MA) all include a significant transition at 9-8 kyrs BP from
263 abundant conifer tree species, such as *Picea* and *Pinus* (green shading, Figure 4) to broadleaved
264 deciduous species, such as *Quercus* (maroon shading, Figure 4). During the past 8 kyrs, *Quercus*
265 pollen was most abundant in southeastern Massachusetts at Deep-Taunton Pond as well as at
266 Crooked Pond (Shuman et al., 2001), but *Betula* and *Fagus* pollen became important at the three
267 mixed forest sites, Heart Lake, Twin Ponds, and Blanding Lake (Figure 4). At these sites, *Tsuga*
268 also remained an important conifer after 8 kyr B.P. (light green, Figure 4), but all four pollen
269 records capture a sharp decline in *Tsuga* abundance from ca. 5.5-3 kyrs B.P. when deciduous
270 angiosperms became most abundant across the region. Afterwards, some conifer taxa, such
271 *Tsuga* and *Pinus*, increased in abundance but never recovered the dominance observed before 8
272 kyrs B.P. Grass (Poaceae) and sage (Cyperaceae) pollen remained low throughout the records
273 indicating the dominance of forests until the historic land clearance of the past 300 yrs.

274 Regionally, the dominant conifers of Late Pleistocene and Early Holocene vegetation
275 suggest a cold and dry climate during the Early Holocene (Webb et al., 1993). The major shift in
276 vegetation from conifer forests to deciduous forests by 8 ka is consistent with a change towards a
277 warm and wet climate during most of the Holocene after the progressive demise of LIS (Shuman
278 et al., 2002). Consistent with lake-level reconstructions from the region (Shuman and Burrell,
279 2017), the increased abundance of mesic (highly moisture-dependent) taxa, such as *Betula*,
280 *Fagus*, and *Tsuga* indicate an increase in regional moisture availability after 9-8 kyrs B.P. (Webb
281 et al., 1993; Marsicek et al., 2013; Shuman et al., 2019),

282 **3.3. Pollen-inferred precipitation seasonality**

283 Changes in precipitation inputs reconstructed using the modern analog technique show
284 sub-regional coherency and major seasonality changes over the past 14 kyrs (Figure 5). Late
285 Pleistocene and Early Holocene precipitation inputs were lower than today (yellow lines are
286 lower than black lines in Figure 5), while Late Pleistocene and Early Holocene (yellow lines,
287 Figure 5) precipitation inputs are characterized by greater precipitation seasonality compared to
288 modern (black lines, Figure 5). Furthermore, the increase in Holocene precipitation inputs was
289 smaller during the summer months than during the winter months. Early Holocene precipitation
290 regimes across the entire region appear to have been dominated by summer precipitation inputs,
291 similar to the modern precipitation inputs observed in the inland areas of New York and
292 Vermont today (Figure 5).

293 In contrast, the Mid- to Late Holocene is characterized by low precipitation seasonality as
294 winter months precipitation inputs increased substantially during the Holocene (Figure 5).
295 Eastern and coastal areas in Pennsylvania and Massachusetts have undergone the largest changes
296 in precipitation seasonality over the past 14 kyrs. Both regions show increases of >70 mm during
297 winter months and an increase of <40 mm during summer months. In comparison, the sites in
298 New York and Vermont show an increase in winter precipitation of ~50 mm/month and an
299 increase in summer precipitation of ~35 mm/month (Figure 5).

300 **3.4. Pollen-inferred hydroclimate trends**

301 Time series of pollen-inferred seasonal precipitation changes reveal several important
302 details on the time evolution of regional hydroclimate (Figure 6A). The reconstructions show
303 three distinctive hydroclimate features: (1) a wet Younger-Dryas interval (12.9-11.7 ka), more
304 prominent at the northern sites (NY and VT) than at the southern or coastal sites (PA and MA),
305 which is consistent with other lines of evidence for increased precipitation during this time

306 interval in the region (Grigg et al., 2021); (2) a region-wide dry Early Holocene (11.7-8.2 ka);
307 and (3) a progressive increase in precipitation during the Mid- to Late Holocene (>6 ka-present)
308 particularly in Massachusetts near the North Atlantic coast and not in Vermont. The entire region
309 has seen a reduction in the warm/cold season ratio of precipitation such that seasonal
310 precipitation inputs are close to being equal during the Late Holocene. In contrast, Early
311 Holocene warm season precipitation inputs were twice those of the cold season (Figure 6B).

312 These precipitation trends are attributable to a combination of global to regional drivers
313 that widely differentiated the climates of portions of the Holocene (Walker et al., 2018). Global
314 influences included changes in insolation and greenhouse gases (Berger, 1978; Indermühle et al.,
315 1999), which increased aridity in many mid-latitude regions in the Early- and Mid-Holocene
316 (Routson et al., 2019). Regional influences included ocean circulation changes during the
317 Younger Dryas interval (McManus et al., 2004) and the presence of the ice sheet until ca. 8 ka
318 (Dyke, 2004). Both factors could have altered advection of moisture into the region. During the
319 Younger Dryas interval, sea surface temperature changes over the North Atlantic may have
320 temporarily altered the storm track along the east coast of North America, delivering increased
321 moisture in the region (Kirby et al., 2002). Equally, the persistence of a glacial anti-cyclone over
322 the ice sheet until ca. 8 ka would have limited the northward advection of moisture into the
323 region (Shuman et al., 2002).

324 The regional increase in seasonal precipitation after the demise of the LIS coincides with
325 precipitation changes elsewhere, including enhanced aridity in the mid-continent (Williams et al.,
326 2010) and effects on the North American monsoon (Bhattacharya et al., 2018). The broad
327 changes across North America indicate an extensive LIS influence on atmospheric circulation
328 and moisture transport, which were part of a set of global changes differentiating the Early- and

329 Mid-Holocene (Walker et al., 2018). The loss of the ice sheet is perhaps the single largest driver
330 behind the rapid increase in precipitation inputs across northeastern U.S. between Early and Mid-
331 Holocene (Shuman et al., 2002), while other factors such as insolation anomalies and internal
332 variability including changes in the Pacific/North American teleconnection pattern probably
333 drove precipitation changes into the Late Holocene (Liu et al., 2014; Shuman and Marsicek,
334 2016).

335 At the inland sites, both cold- and warm-season precipitation increase towards modern
336 values after ~10 ka, but cold-season precipitation increased more than warm-season precipitation
337 (Figure 7). Therefore, both seasons contribute nearly equally from 8 ka to present. At the coastal
338 site of Deep-Taunton, cold-season precipitation inputs during the late Pleistocene were ~40%
339 lower than modern. At this site, cold-season precipitation inputs after 8 ka increased further by
340 another ~30%. In contrast, this coastal site saw little change in warm-season precipitation inputs
341 during the past 14 kyrs (~15% of modern).

342 **3.5. Modeled $\delta^2\text{H}_{\text{MAP}}$ values during the past 14 kyrs**

343 The potential impacts of the reconstructed changes in precipitation seasonality on
344 $\delta^2\text{H}_{\text{MAP}}$ were tested using Eq.2. To predict the potential magnitude of $\delta^2\text{H}_{\text{MAP}}$ change related to
345 the changing seasonality of precipitation over the past 14 kyrs. we combined modern monthly
346 $\delta^2\text{H}$ values (OIPC) from individual pollen sites with pollen-inferred monthly precipitation inputs.
347 The model assumes no change in monthly precipitation $\delta^2\text{H}$ values (i.e., it uses constant modern
348 monthly OIPC $\delta^2\text{H}$ values), and shows that changes in seasonality alone would have caused
349 $\delta^2\text{H}_{\text{MAP}}$ values to peak during the Late Pleistocene (Figure 7B, orange lines). At the time, warm
350 season precipitation inputs were ~20% higher than cold season precipitation inputs, which were
351 at their lowest levels of the past 14 kyrs (40% of modern; Figure 7A). Although modeled $\delta^2\text{H}_{\text{MAP}}$

352 values decreased by ~10‰ across the region during the Holocene as cold season precipitation
353 inputs increased, these modeled values were far more stable than the 10-40% change in seasonal
354 precipitation (compare Figure 7A with orange lines in Figure 7B). These results agree with our
355 modeled expectations of $\delta^2\text{H}_{\text{MAP}}$ values given seasonal changes in precipitation (Figure 3C,D).

356 Coastal sites like Deep-Taunton record larger increases in cold-season precipitation
357 inputs (~60%) compared to the inland sites (Figure 6-7), but modeled and reconstructed cold-
358 season $\delta^2\text{H}$ values are higher along the coast than at the inland sites (Figure 3A). Consequently,
359 the high cold season $\delta^2\text{H}$ values at this site can offset an increase in cold season precipitation
360 inputs creating a continuous decline in $\delta^2\text{H}_{\text{MAP}}$ values spanning over the last 14 kyrs (Figure 3C).
361 These results are also consistent with the modest change in modeled $\delta^2\text{H}_{\text{MAP}}$ values inferred
362 across the region (orange lines, Figure 7B).

363 **3.6. Reconstructed $\delta^2\text{H}_{\text{MAP_C29}}$ values during the past 14 kyrs**

364 Reconstructed $\delta^2\text{H}_{\text{MAP_C29}}$ values have similar magnitudes and directions of change
365 across all sites (Figure 7B, blue lines). The reconstructed trends differ in detail, but except for
366 Twin Ponds, the *n*-C₂₉ records indicate that $\delta^2\text{H}_{\text{MAP_C29}}$ values were ~10‰ more positive than
367 today during Early to Mid-Holocene (Figure 7). Additionally, $\delta^2\text{H}_{\text{MAP_C29}}$ values from New York
368 and Vermont are typically ~20‰ lower than those from Pennsylvania and Massachusetts as
369 expected from the modern isotopic gradients (e.g., as calculated by OPIC; Figure 3A). Although
370 each record also contains unique patterns of high frequency variability of 20-40‰, the long-term
371 trends generally conform with expectations simulated from the pollen data (compare orange and
372 blue lines, Figure 7B).

373 As the model assumes no change in monthly precipitation $\delta^2\text{H}$ values over the past 14
374 kyrs, we hypothesize that the $\delta^2\text{H}_{\text{MAP_C29}}$ trends would have deviated substantially from modeled
375 $\delta^2\text{H}_{\text{MAP}}$ values if changes in moisture sources, pathways, or in soil evaporation regimes occurred
376 in the past. The similarity between modeled and reconstructed $\delta^2\text{H}_{\text{MAP}}$ values suggests that the
377 LIS presence limited the advection of subtropical moisture into the region and created extremely
378 low annual precipitation inputs during the Early Holocene. However, as proposed by Schartman
379 et al. (2020), we find that moisture sources in the region remained the same. Moreover, if warm
380 summers and high summer insolation during Early and Mid-Holocene affected soil water $\delta^2\text{H}$
381 values by enhancing evaporation, then the reconstructed $\delta^2\text{H}_{\text{MAP_C29}}$ values would have been
382 consistently more positive than the pollen-inferred $\delta^2\text{H}_{\text{MAP}}$ values. Yet the $\delta^2\text{H}_{\text{MAP_C29}}$ records are
383 either within or below the range of modeled $\delta^2\text{H}_{\text{MAP}}$ values, which indicates that soil evaporation
384 did not play a major role in modifying soil moisture $\delta^2\text{H}$ values.

385 Consequently, our results show that the region's hydroclimate was likely modulated by
386 the LIS presence and associated high-pressure, anticyclone atmospheric movements during the
387 Early Holocene (Shuman et al., 2002). However, after the demise of the LIS, the change in the
388 frequency of northward advection of moisture especially during the winter did not substantially
389 alter moisture sources and pathways (Figure 5 and 6). Furthermore, unless Early Holocene soil
390 evaporation closely offset a negative shift in $\delta^2\text{H}$ values driven by changes in atmospheric
391 circulation, our $\delta^2\text{H}_{\text{MAP_C29}}$ records and pollen-derived sensitivity test indicate that neither
392 process dramatically changed $\delta^2\text{H}_{\text{MAP}}$ values despite the large climate forcing involved. With the
393 progressive demise and final LIS collapse by ~ 8 ka, the region experienced major increases in
394 seasonal precipitation inputs, but the relative balance of changes across seasons produced only
395 small changes in $\delta^2\text{H}_{\text{MAP}}$ values (Figures 5-7). Therefore, these results confirm that $\delta^2\text{H}_{\text{MAP_C29}}$ is

396 sensitive to and tracks major changes in $\delta^2\text{H}_{\text{MAP}}$, but the combined effects of seasonal changes in
397 precipitation can reduce the amplitude of $\delta^2\text{H}_{\text{MAP}}$ signals compared to the associated seasonal
398 precipitation changes (Figure 7). Interpretation of leaf-wax $\delta^2\text{H}$ records, therefore, can benefit
399 from comparison with other hydroclimate reconstructions.

400 In addition to the major trends, the pollen-inferred precipitation regimes suggest century-
401 scale variability across the region (Figs. 6 and 7), which is closely replicated by evidence for
402 lake-level changes from the northeastern U.S. (Shuman et al., 2019). However, when monthly
403 precipitation reconstructions were converted to $\delta^2\text{H}_{\text{MAP}}$ values using Eq. 2 (orange lines, Figure
404 7B), the century-scale variability – and longer events such as the anomalously high precipitation
405 during the Younger Dryas – were not detected. The lack of century-scale variability in modeled
406 $\delta^2\text{H}_{\text{MAP}}$ values arises, in isotope space, for the same reason that the long-term trends experienced
407 only small changes in $\delta^2\text{H}_{\text{MAP}}$ values: even large percentage changes in total precipitation
408 produce small net changes in $\delta^2\text{H}_{\text{MAP}}$ values (Figure 3). This is especially the case when the same
409 direction of precipitation change occurs in different seasons, yielding opposite isotopic direction
410 of changes that cancel each other. Moreover, the $\delta^2\text{H}_{\text{MAP_C29}}$ records indicate large centennial-
411 scale isotopic variability, but this variability is neither consistent with the patterns expected from
412 the pollen nor consistent across sites (Figure 7B). This centennial isotopic variability could
413 represent shifts in precipitation sources as the reconstructed values exceed the calibration
414 uncertainty (1 s.d.=12‰; Stefanescu et al., 2023). However, the low temporal resolution of our
415 $n\text{-C}_{29}$ records prevents us from making inferences about centennial scale shifts in precipitation
416 sources. Twin Ponds (VT) may highlight one of the most extreme examples of other potential
417 influences.

418 **3.7. $\delta^2\text{H}_{\text{MAP_C29}}$ anomaly at Twin Ponds, Vermont**

419 The Twin Ponds $\delta^2\text{H}_{\text{MAP_C29}}$ record shows a substantial deviation from modeled $\delta^2\text{H}_{\text{MAP}}$
420 values and regional $\delta^2\text{H}_{\text{MAP_C29}}$ patterns (Figure 7B). However, the two New York $\delta^2\text{H}_{\text{MAP_C29}}$
421 records (Figure 7B, Schartman et al., 2020) do not show the same anomaly and are inconsistent
422 with a regional change in circulation pathways or sources across the northern part of the region.
423 Due to the geographic proximity and climate similarity of Twin Ponds and the two New York
424 sites, we infer that this particular sediment record was likely influenced by lake specific
425 variations, such as changes in *n*-C₂₉-alkane source.

426 Pollen-inferred vegetation changes at and near our sites (Figure 4) show a shift from a
427 gymnosperm- to an angiosperm-dominated vegetation during the Holocene. Average
428 fractionation factors between *n*-C₂₉-alkane and precipitation $\delta^2\text{H}$ values are comparable for
429 gymnosperms and angiosperms (within 6‰; Stefanescu et al., 2023). Moreover, the vegetation
430 shift is not unique to Twin Ponds (Figure 4). Therefore, the Early Holocene vegetation transition
431 is an unlikely explanation for the prolonged negative anomaly in $\delta^2\text{H}_{\text{MAP_C29}}$ values at Twin
432 Ponds.

433 Even though *n*-C₂₉-alkane is predominantly synthesized by terrestrial plants, aquatic
434 plants can also synthesize *n*-C₂₉-alkane in small amounts and could be an additional source of
435 unusual isotopic values. An aquatic source may be particularly important at Twin Ponds where
436 our primary core was collected from a productive littoral bench distal from the inlet, at a shallow
437 depth of only 0.79 m. The fractionation factor between the aquatically produced *n*-C₂₉-alkane
438 and $\delta^2\text{H}_{\text{MAP}}$ (ϵ_{app}) is ~30‰ larger than that of terrestrial plants (Stefanescu et al., 2023),
439 therefore, a shift to aquatically produced *n*-alkanes would generate a negative excursion in
440 reconstructed $\delta^2\text{H}_{\text{MAP_C29}}$ values at Twin Ponds. Littoral terrestrial vegetation such as grasses
441 may also be an important additional source. ϵ_{app} in grasses is also ~30‰ larger than in terrestrial

442 plants (Stefanescu et al., 2023) and, therefore, *n*-C₂₉ compounds derived from grasses would also
443 generate a negative excursion in reconstructed $\delta^2\text{H}_{\text{MAP_C29}}$ values.

444 To evaluate the potential role of alternative *n*-C₂₉-alkane sources within the lake, we
445 measured *n*-C₂₉ $\delta^2\text{H}$ values in four sediment samples derived from the deep-water core collected
446 at a depth of 7.8 m from Twin Ponds (Figure 7B; black squares). $\delta^2\text{H}$ values for these four
447 samples spanning over the Mid-Holocene differ significantly from the $\delta^2\text{H}_{\text{MAP_C29}}$ trends
448 observed in the shallow core (blue line, Figure 7B). Furthermore, the reconstructed $\delta^2\text{H}_{\text{MAP_C29}}$
449 values fall within the range of modeled $\delta^2\text{H}_{\text{MAP}}$ based on the pollen data (orange lines, Figure
450 7B). Despite the small number of samples derived from the deep-water core, the data shows
451 major differences in $\delta^2\text{H}_{\text{MAP_C29}}$ values between the shallow and deep-water cores, as well as in
452 the long-term $\delta^2\text{H}_{\text{MAP_C29}}$ trends. Given that proximity to shore can drive a dominant aquatic and
453 grass input of *n*-C₂₉-alkane into lake sediments, and that both aquatic plants and grasses have
454 higher ϵ_{app} values compared to those of higher terrestrial plants, we infer that the negative
455 excursion in reconstructed $\delta^2\text{H}_{\text{MAP_C29}}$ values in the shallow-water core at Twin Ponds was
456 driven by increased aquatic or grass inputs. Further analysis is needed to quantify *n*-C₂₉-alkane
457 sources and their $\delta^2\text{H}$ values in the deep-water core in order to assess the amount of aquatic and
458 grass input and its effects on *n*-C₂₉ $\delta^2\text{H}$ values within lakes.

459 4. CONCLUSIONS

460 Our new leaf-wax $\delta^2\text{H}$ records from the northeastern U.S. suggest a small change in
461 $\delta^2\text{H}_{\text{MAP}}$ values over the past 14 kyrs. The new *n*-alkane data agree with other, previously
462 published records (Puleo et al., 2020; Schartman et al., 2020) and indicate little change in mean
463 annual precipitation $\delta^2\text{H}$ values ($\delta^2\text{H}_{\text{MAP}}$) during a major regional climate transition. The lack of
464 major changes in $\delta^2\text{H}_{\text{MAP}}$ values poses a fascinating paradox, which we resolve by combining the

465 modern distribution of monthly $\delta^2\text{H}$ values with the pollen-inferred changes in seasonal
466 precipitation inputs to model the expected changes in $\delta^2\text{H}_{\text{MAP}}$ values given seasonality changes in
467 precipitation inputs over the past 14 kyrs. Our model generates Holocene $\delta^2\text{H}_{\text{MAP}}$ expectations
468 given only the reconstructed shifts in the seasonality of precipitation and does not account for
469 changes in moisture sources, moisture pathways, or soil moisture evaporation, which may have
470 influenced $\delta^2\text{H}_{\text{MAP_C29}}$. The resulting agreement in the predicted $\delta^2\text{H}_{\text{MAP}}$ patterns and those
471 measured with our new $\delta^2\text{H}_{\text{MAP_C29}}$ records confirm that, although precipitation increased across
472 the region, $\delta^2\text{H}_{\text{MAP}}$ decreased by only 10‰ due to a shift in the seasonality of precipitation.

473 We hypothesize that the LIS presence and associated anti-cyclone during the Late
474 Pleistocene and Early Holocene likely prevented the advection of moisture into the region
475 especially during the winter. The pattern explains the low precipitation rates inferred from the
476 pollen data, except when unusual conditions over the North Atlantic favored high precipitation
477 during the Younger Dryas. However, neither change produced large variations in the isotopic
478 values of regional precipitation. Subsequently, the progressive demise of the LIS by 8 ka allowed
479 cold-season precipitation to increase such that both cold- and warm-season precipitation fell
480 more equally across the region since 8 ka. However, these seasonal changes in precipitation,
481 which affected both the vegetation and regional lake levels, translated to only minor changes in
482 $\delta^2\text{H}_{\text{MAP}}$ values. These results suggest that precipitation inputs in the region were not modulated
483 by changes in moisture sources or moisture pathways over the past 14 kyrs. Consequently, our
484 results show that $\delta^2\text{H}_{\text{MAP_C29}}$ records are sensitive to $\delta^2\text{H}_{\text{MAP}}$ changes in the mid-latitudes, but
485 changes in $\delta^2\text{H}_{\text{MAP}}$ values can be dampened by counterbalancing shifts in seasonal precipitation
486 changes. Similar seasonal precipitation shifts may dampen the isotopic signature of other
487 hydroclimate changes in this and other regions, particularly those with highly seasonal

488 precipitation elsewhere in the mid-latitudes. Therefore, seasonal precipitation changes would be
489 valuable to assess when interpreting stable isotopic records of mean annual precipitation.

490 **ACKNOWLEDGMENTS**

491 We thank Dr. Josef P. Werne and an anonymous reviewer for their comments and
492 suggestions that greatly improved our manuscript. We thank Chandelle Macdonald and Craig
493 Cook for help with GC-IRMS analyses. This work was supported by the National Science
494 Foundation Grant 1146297 and EPS-1655726. Adriana Bailey acknowledges support from the
495 National Center for Atmospheric Research, which is a major facility sponsored by the National
496 Science Foundation under Cooperative Agreement 1852977.

497 **DATA AVAILABILITY**

498 Data associated with this article can be accessed at <https://doi.org/10.15786/20126495>.

499 **REFERENCES**

- 500 Basu, S., Sanyal, P., Pillai, A.A. and Ambili, A., 2019. Response of grassland ecosystem to
501 monsoonal precipitation variability during the Mid-Late Holocene: Inferences based on
502 molecular isotopic records from Banni grassland, western India. *PLoS one*, 14(4),
503 p.e0212743.
- 504 Berger, A., 1978. Long-term variations of daily insolation and Quaternary climatic changes.
505 *Journal of Atmospheric Sciences*, 35(12), pp.2362-2367.
- 506 Bhattacharya, T., Tierney, J.E., Addison, J.A. and Murray, J.W., 2018. Ice-sheet modulation of
507 deglacial North American monsoon intensification. *Nature Geoscience*, 11(11), pp.848-
508 852.
- 509 Bowen, G. J. 2020: Gridded maps of the isotopic composition of meteoric waters.
510 <http://www.waterisotopes.org>
- 511 Cai, S., and Z. Yu. 2011. Response of a warm temperate peatland to Holocene climate change in
512 northeastern Pennsylvania. *Quaternary Research* 75:531-540.
- 513 Campbell, J. and M. Green. 2019. Water isotope samples from Watershed 3 at Hubbard Brook
514 Experimental Forest, 2006-2010 ver 1. Environmental Data Initiative.
515 <https://doi.org/10.6073/pasta/f5740876b68ec42b695c39d8ad790cee> (Accessed 2021-06-
516 22)
- 517 Cao, M., Sun, J., Liu, W., Hou, J., Tian, Q. and Sun, Z., 2020. Paleoclimatic fluctuations inferred
518 from leaf wax n-alkane records in Central Tibet in the late Oligocene to early
519 Miocene. *Palaeogeography, Palaeoclimatology, Palaeoecology*, 539, p.109504.

520 Craig H. 1961. Isotopic variations in meteoric waters. *Science* 133:1702–3 Craig
521 Dansgaard, W., 1964. Stable isotopes in precipitation. *Tellus*, 16(4), pp.436-468.

522 Dyke, A.S., 2004. An outline of North American deglaciation with emphasis on central and
523 northern Canada. *Developments in quaternary sciences*, 2, pp.373-424.

524 Faegri, K. and Iversen, J. (1975) *Textbook of Pollen Analysis*. Munksgaard, Copenhagen.

525 Freimuth, E.J., Diefendorf, A.F., Lowell, T.V., 2017. Hydrogen isotopes of n-alkanes and n-
526 alkanolic acids as tracers of precipitation in a temperate forest and im- plications for
527 paleorecords. *Geochim. Cosmochim. Acta* 206, 166e183. [https://](https://doi.org/10.1016/j.gca.2017.02.027)
528 doi.org/10.1016/j.gca.2017.02.027.

529 Gao, L., Huang, Y., Shuman, B., Oswald, W.W. and Foster, D., 2017. A high-resolution
530 hydrogen isotope record of behenic acid for the past 16 kyr in the northeastern United
531 States. *Quaternary International*, 449, pp.1-11.

532 Garcin, Y., Schwab, V.F., Gleixner, G., Kahmen, A., Todou, G., Séné, O., Onana, J.M.,
533 Achoundong, G. and Sachse, D., 2012. Hydrogen isotope ratios of lacustrine sedimentary
534 n-alkanes as proxies of tropical African hydrology: insights from a calibration transect
535 across Cameroon. *Geochimica et Cosmochimica Acta*, 79, pp.106-126.

536 Gat, J.R., 1996. Oxygen and hydrogen isotopes in the hydrologic cycle. *Annual Review of Earth*
537 *and Planetary Sciences*, 24, pp.225-262.

538 Craig, H., 1961. Isotopic variations in meteoric waters. *Science*, 133(3465), pp.1702-1703.

539 Grigg, L.D., Engle, K.J., Smith, A.J., Shuman, B.N. and Mandl, M.B., 2021. A multi-proxy
540 reconstruction of climate during the late-Pleistocene to early Holocene transition in the
541 northeastern, USA. *Quaternary Research*, pp.1-17.

542 Haslett J, Parnell AC, 2008. “A simple monotone process with application to radiocarbon-dated
543 depth chronologies.” *Journal of the Royal Statistical Society: Series C (Applied*
544 *Statistics)*, **57**(4), 399–418. [https://rss.onlinelibrary.wiley.com/doi/full/10.1111/j.1467-](https://rss.onlinelibrary.wiley.com/doi/full/10.1111/j.1467-9876.2008.00623.x)
545 [9876.2008.00623.x](https://rss.onlinelibrary.wiley.com/doi/full/10.1111/j.1467-9876.2008.00623.x).

546 Hou, J., Huang, Y., Oswald, W.W., Foster, D.R. and Shuman, B., 2007. Centennial-scale
547 compound-specific hydrogen isotope record of Pleistocene–Holocene climate transition
548 from southern New England. *Geophysical Research Letters*, 34(19).

549 Ibe, R.A. 1982. Quaternary palynology of five lacustrine deposits in the Catskill Mountain
550 region of New York. Dissertation. New York University, New York, New York, USA.

551 Indermühle, A., Stocker, T.F., Joos, F., Fischer, H., Smith, H.J., Wahlen, M., Deck, B.,
552 Mastroianni, D., Tschumi, J., Blunier, T. and Meyer, R., 1999. Holocene carbon-cycle
553 dynamics based on CO₂ trapped in ice at Taylor Dome, Antarctica. *Nature*, 398(6723),
554 pp.121-126.

555 Kirby, M.E., Mullins, H.T., Patterson, W.P. and Burnett, A.W., 2002. Late glacial–Holocene
556 atmospheric circulation and precipitation in the northeast United States inferred from
557 modern calibrated stable oxygen and carbon isotopes. *Geological Society of America*
558 *Bulletin*, 114(10), pp.1326-1340.

559 Liu, Z., Yoshimura, K., Bowen, G.J., Buening, N.H., Risi, C., Welker, J.M. and Yuan, F., 2014.
560 Paired oxygen isotope records reveal modern North American atmospheric dynamics
561 during the Holocene. *Nature communications*, 5(1), pp.1-7.

562 Mandl, M.B., Shuman, B.N., Marsicek, J. and Grigg, L., 2016. Estimating the regional climate
563 signal in a late Pleistocene and early Holocene lake-sediment $\delta^{18}\text{O}$ record from Vermont,
564 USA. *Quaternary Research*, 86(1), pp.67-78.

565 Marsicek, J.P., Shuman, B., Brewer, S., Foster, D.R. and Oswald, W.W., 2013. Moisture and
566 temperature changes associated with the mid-Holocene *Tsuga* decline in the northeastern
567 United States. *Quaternary Science Reviews*, 80, pp.129-142.

568 McFarlin, J.M., Axford, Y., Masterson, A.L. and Osburn, M.R., 2019. Calibration of modern
569 sedimentary $\delta^2\text{H}$ plant wax-water relationships in Greenland lakes. *Quaternary Science*
570 *Reviews*, 225, p.105978.

571 McManus, J.F., Francois, R., Gherardi, J.M., Keigwin, L.D. and Brown-Leger, S., 2004.
572 Collapse and rapid resumption of Atlantic meridional circulation linked to deglacial
573 climate changes. *nature*, 428(6985), pp.834-837.

574 Newby, P.E., Shuman, B.N., Donnelly, J.P. and MacDonald, D., 2011. Repeated century-scale
575 droughts over the past 13,000 yr near the Hudson River watershed, USA. *Quaternary*
576 *Research*, 75(3), pp.523-530.

577 Oswald, W.W., Foster, D.R., Shuman, B.N., Doughty, E.D., Faison, E.K., Hall, B.R., Hansen,
578 B.C., Lindbladh, M., Marroquin, A. and Truebe, S.A., 2018. Subregional variability in
579 the response of New England vegetation to postglacial climate change. *Journal of*
580 *biogeography*, 45(10), pp.2375-2388.

581 Overpeck, J.T., Webb III, T. and Prentice, I.C., 1985. Quantitative interpretation of fossil pollen
582 spectra: dissimilarity coefficients and the method of modern analogs. *Quaternary*
583 *Research*, 23(1), pp.87-108.

584 Parnell, A.C., Haslett, J., Allen, J.R., Buck, C.E., Huntley, B., 2008. A flexible approach to
585 assessing synchronicity of past events using Bayesian reconstructions of sedimentation
586 history. *Quaternary Science Reviews* 27, 1872–1885.

587 PRISM Climate Group, Oregon State University, <http://prism.oregonstate.edu>, created June 2021

588 Puleo, P.J., Axford, Y., McFarlin, J.M., Curry, B.B., Barklage, M. and Osburn, M.R., 2020. Late
589 glacial and Holocene paleoenvironments in the midcontinent United States, inferred from
590 Geneva Lake leaf wax, ostracode valve, and bulk sediment chemistry. *Quaternary*
591 *Science Reviews*, 241, p.106384.

592 Rach, O., Brauer, A., Wilkes, H. and Sachse, D., 2014. Delayed hydrological response to
593 Greenland cooling at the onset of the Younger Dryas in western Europe. *Nature*
594 *Geoscience*, 7(2), pp.109-112.

595 Reimer, P.J., Austin, W.E., Bard, E., Bayliss, A., Blackwell, P.G., Ramsey, C.B., Butzin, M.,
596 Cheng, H., Edwards, R.L., Friedrich, M. and Grootes, P.M., 2020. The IntCal20 Northern
597 Hemisphere radiocarbon age calibration curve (0–55 cal kBP). *Radiocarbon*, 62(4),
598 pp.725-757.

599 Routson, C.C., McKay, N.P., Kaufman, D.S., Erb, M.P., Goosse, H., Shuman, B.N., Rodysill,
600 J.R. and Ault, T., 2019. Mid-latitude net precipitation decreased with Arctic warming
601 during the Holocene. *Nature*, 568(7750), pp.83-87.

602 Sachse, D., Radke, J. and Gleixner, G., 2004. Hydrogen isotope ratios of recent lacustrine
603 sedimentary n-alkanes record modern climate variability. *Geochimica et Cosmochimica*
604 *Acta*, 68(23), pp.4877-4889.

605 Sachse, D., Radke, J. and Gleixner, G., 2006. δD values of individual n-alkanes from terrestrial
606 plants along a climatic gradient—Implications for the sedimentary biomarker record.
607 *Organic Geochemistry*, 37(4), pp.469-483.

608 Sachse, D., Billault, I., Bowen, G.J., Chikaraishi, Y., Dawson, T.E., Feakins, S.J., Freeman,
609 K.H., Magill, C.R., McInerney, F.A., van der Meer, M.T.J.J., Polissar, P., Robins, R.J.,
610 Sachs, J.P., Schmidt, H.-L., Sessions, A.L., White, J.W.C., West, J.B., Kahmen, A., 2012.
611 Molecular paleohydrology: interpreting the hydrogen- isotopic composition of lipid
612 biomarkers from photosynthesizing organisms. *Annu. Rev. Earth Planet. Sci.* 40,
613 221e249. <https://doi.org/10.1146/annurev-earth-042711-105535>.

614 Schartman, A.K., Diefendorf, A.F., Lowell, T.V., Freimuth, E.J., Stewart, A.K., Landis, J.D. and
615 Bates, B.R., 2020. Stable source of Holocene spring precipitation recorded in leaf wax
616 hydrogen-isotope ratios from two New York lakes. *Quaternary Science Reviews*, 240,
617 p.106357.

618 Schefuß, E., Schouten, S. and Schneider, R.R., 2005. Climatic controls on central African
619 hydrology during the past 20,000 years. *Nature*, 437(7061), pp.1003-1006.

620 Shuman, B., Bravo, J., Kaye, J., Lynch, J.A., Newby, P. and Webb, T., 2001. Late Quaternary
621 water-level variations and vegetation history at Crooked Pond, southeastern
622 Massachusetts. *Quaternary Research*, 56(3), pp.401-410.

623 Shuman, B., Bartlein, P., Logar, N., Newby, P. and Webb III, T., 2002. Parallel climate and
624 vegetation responses to the early Holocene collapse of the Laurentide Ice Sheet.
625 *Quaternary science reviews*, 21(16-17), pp.1793-1805.

626 Shuman, B. and Donnelly, J.P., 2006. The influence of seasonal precipitation and temperature
627 regimes on lake levels in the northeastern United States during the Holocene. *Quaternary*
628 *Research*, 65(1), pp.44-56.

629 Shuman, B., Huang, Y., Newby, P. and Wang, Y., 2006. Compound-specific isotopic analyses
630 track changes in seasonal precipitation regimes in the Northeastern United States at ca
631 8200 cal yr BP. *Quaternary Science Reviews*, 25(21-22), pp.2992-3002.

632 Shuman, B.N., Newby, P. and Donnelly, J.P., 2009. Abrupt climate change as an important agent
633 of ecological change in the Northeast US throughout the past 15,000 years. *Quaternary*
634 *Science Reviews*, 28(17-18), pp.1693-1709.

635 Shuman, B. and Plank, C., 2011. Orbital, ice sheet, and possible solar controls on Holocene
636 moisture trends in the North Atlantic drainage basin. *Geology*, 39(2), pp.151-154.

637 Shuman, B.N. and Marsicek, J., 2016. The structure of Holocene climate change in mid-latitude
638 North America. *Quaternary Science Reviews*, 141, pp.38-51.

639 Shuman, B.N. and Burrell, S.A., 2017. Centennial to millennial hydroclimatic fluctuations in the
640 humid northeast United States during the Holocene. *Quaternary Research*, 88(3), pp.514-
641 524.

642 Shuman, B.N., Marsicek, J., Oswald, W.W. and Foster, D.R., 2019. Predictable hydrological and
643 ecological responses to Holocene North Atlantic variability. *Proceedings of the National*
644 *Academy of Sciences*, 116(13), pp.5985-5990.

645 Stefanescu, I.C., Macdonald, C., Cook, C.S., Williams, D.G. and Shuman, B.N., 2023. Mid-and
646 long-chain leaf wax $\delta^2\text{H}$ values in modern plants and lake sediments from mid-latitude
647 North America. *Geochimica et Cosmochimica Acta*, 340, pp.158-171.

648 Suter, S.M. 1985. Late-glacial and Holocene vegetation history in southeastern Massachusetts: a
649 14,000 year pollen record. *Current Research in the Pleistocene*. *Current Research in the*
650 *Pleistocene* 2:87-89.

651 Tierney, J.E., Russell, J.M. and Huang, Y., 2010. A molecular perspective on Late Quaternary
652 climate and vegetation change in the Lake Tanganyika basin, East Africa. *Quaternary*
653 *Science Reviews*, 29(5-6), pp.787-800.

654 Tipple, B.J., Berke, M.A., Doman, C.E., Khachatryan, S., Ehleringer, J.R., 2013. Leaf- wax n-
655 alkanes record the plant-water environment at leaf flush. *Proc. Natl. Acad. Sci.* 110,
656 2659e2664. <https://doi.org/10.1073/pnas.1213875110>.

657 Toney, J.L., García-Alix, A., Jiménez-Moreno, G., Anderson, R.S., Moossen, H. and Seki, O.,
658 2020. New insights into Holocene hydrology and temperature from lipid biomarkers in
659 western Mediterranean alpine wetlands. *Quaternary Science Reviews*, 240, p.106395.

660 Walker, M., Head, M.J., Lowe, J., Berkelhammer, M., Björck, S., Cheng, H., Cwynar, L.C.,
661 Fisher, D., Gkinis, V., Long, A. and Newnham, R., 2019. Subdividing the Holocene
662 Series/Epoch: formalization of stages/ages and subseries/subepochs, and designation of
663 GSSPs and auxiliary stratotypes. *Journal of Quaternary Science*, 34(3), pp.173-186.

664 Webb, R.S., Anderson, K.H. and Webb III, T., 1993. Pollen response-surface estimates of late-
665 Quaternary changes in the moisture balance of the northeastern United States. *Quaternary*
666 *Research*, 40(2), pp.213-227.

667 White, J.M., R.W. Mathewes, and W.H. Mathews. 1985. Late Pleistocene chronology and
668 environment of the "ice-free corridor" of northwestern Alberta. *Quaternary Research*
669 24:173-186.

670 Whitehead, D.R., and S.T. Jackson. 1990. The regional vegetational history of the High Peaks
671 (Adirondack Mountains), New York. Bulletin No. 478, New York State Museum,
672 Albany, New York, USA.

673 Whitmore, J., Gajewski, K., Sawada, M., Williams, J.W., Shuman, B., Bartlein, P.J., Minckley,
674 T., Viau, A.E., Webb III, T., Shafer, S. and Anderson, P., 2005. Modern pollen data from
675 North America and Greenland for multi-scale paleoenvironmental
676 applications. *Quaternary Science Reviews*, 24(16-17), pp.1828-1848.

677 Williams, J.W. and Shuman, B., 2008. Obtaining accurate and precise environmental
678 reconstructions from the modern analog technique and North American surface pollen
679 dataset. *Quaternary Science Reviews*, 27(7-8), pp.669-687.

680 Williams, J.W., Shuman, B., Bartlein, P.J., Diffenbaugh, N.S. and Webb III, T., 2010. Rapid,
681 time-transgressive, and variable responses to early Holocene midcontinental drying in
682 North America. *Geology*, 38(2), pp.135-138.

683 Williams, J.W., Grimm, E.C., Blois, J.L., Charles, D.F., Davis, E.B., Goring, S.J., Graham,
684 R.W., Smith, A.J., Anderson, M., Arroyo-Cabrales, J. and Ashworth, A.C., 2018. The
685 Neotoma Paleoecology Database, a multiproxy, international, community-curated data
686 resource. *Quaternary Research*, 89(1), pp.156-177.

Site	Analysis	Latitude	Longitude	Elevation m	MAP mm	MAP $\delta^2\text{H}\%$	MAAT °C	Citation
Brandreth Bog (NY)	pollen	43.917	-74.683	582	1193	-74	4.9.0	Overpeck, J.T. 1985
Heart Lake (NY)	pollen <i>n</i> -C ₂₉	44.182	-73.970	665	1137	-76	5.0	Whitehead and Jackson 1990 Schartman et al., 2020
Moose Lake (NY)	<i>n</i> -C ₂₉	44.370	-74.060	475	1075	-74	5.1	Schartman et al., 2020
Balsam Lake (NY)	pollen	42.029	-74.604	880	1381	-64	5.0	Ibe, R.A. 1982
Knob Hill (VT)	pollen	44.360	-72.373	378	1015	-70	5.7	Oswald et al., 2018
Twin Ponds (VT)	pollen <i>n</i> -C ₂₉	44.061	-72.579	409	1072	-69	5.5	This study
Blanding Pond (PA)	pollen <i>n</i> -C ₂₉	41.798	-75.676	454	1127	-59	7.6	This study
Spring Lake (PA)	pollen	41.674	-76.350	364	960	-60	8.2	White et al., 1985
Hubbard Brook (NH)	precipitation soil	43.779	-71.725	755	1129	-71	6.6	Campbell and Green, 2019
Black Pond (MA)	pollen	41.328	-70.793	13	1213	-43	10.4	Oswald et al., 2018
Crooked Pond (MA)	<i>n</i> -C ₂₉	41.887	-70.646	45	1274	-46	9.9	This study
Deep- Falmouth Pond (MA)	pollen	41.564	-70.636	27	1260	-48	10.4	Oswald et al., 2018
Deep- Taunton Pond (MA)	pollen	41.882	-71.012	8	1260	-47	10	Oswald et al., 2018
Tannersville Bog (PA)	pollen	41.039	-75.264	282	1307	-51	9.2	Cai and Yu, 2011
Uncle Seth's Pond (MA)	pollen	41.433	-70.665	20	1251	-43	10.4	Oswald et al., 2018
Upper Wallface Pond (NY)	pollen	44.148	-74.056	981	1413	-80	3.7	Whitehead and Jackson, 1990
Winneconnet Pond	pollen	41.967	-71.117	22	1265	-48	10.0	Suter, S.M. 1985.

687 **Table 1.** Site locations and modern environmental parameters.

688 **Table 2.** Radiocarbon analyses.

Lake	Depth (m)	Thickness (cm)	Lab No.	Material	¹⁴ C yr B.P.	Error (yr)	Calibrated age range B.P.		
							5%	Median	95%
Twin Ponds	42	2	UCIAMS-127563	Charcoal	1530	15	1365	1391	1454
Twin Ponds	76.5*	1	UCIAMS-127562	Charcoal	430	15	482	499	509
Twin Ponds	162.5	1	UCIAMS-127561	Charcoal	3040	25	3177	3248	3332
Twin Ponds	266.5	1	UCIAMS-127560	Charcoal	4225	25	4659	4758	4841
Twin Ponds	386.5**	2	UCIAMS-121904	core 48	9970	60	11273	11438	11684
Twin Ponds	414.5**	2	UCIAMS-121905	core 48	11070	40	12900	13000	13080
Blanding Lake	73	2	UCIAMS-190318	Charcoal	625	45	550	602	656
Blanding Lake	133	2	UCIAMS-190319	Charcoal	2225	35	2150	2226	2323
Blanding Lake	250	2	UCIAMS-190320	Charcoal	3450	70	3551	3709	3862
Blanding Lake	328	1	UCIAMS-190321	Charcoal	4280	20	4835	4847	4860
Blanding Lake	368	1	UCIAMS-190322	Charcoal	4410	20	4885	4977	5043
Blanding Lake	480*	2	UCIAMS-190323	Charcoal	16300	80	19526	19691	19861
Blanding Lake	541	1	UCIAMS-190324	Charcoal	7230	130	7833	8054	8294
Blanding Lake	577	1	UCIAMS-190325	Charcoal	7925	50	8621	8767	8967
Blanding Lake	652	2	UCIAMS-190326	Charcoal	8950	60	9900	10057	10208
Blanding Lake	738	1	UCIAMS-190327	Charcoal	12080	45	13821	13930	14052
Crooked Pond	62	1	UCIAMS-83271	Charcoal	1415	20	1297	1319	1344
Crooked Pond	77	1	UCIAMS-83272	Charcoal	2190	20	2130	2240	2298
Crooked Pond	100	1	UCIAMS-83273	Charcoal	2850	20	2886	2958	3039
Crooked Pond	110	1	UCIAMS-83274	Charcoal	3080	20	3235	3291	3354
Crooked Pond	128	1	UCIAMS-83275	Charcoal	3520	20	3723	3779	3858
Crooked Pond	139	1	UCIAMS-111581	Charcoal	4025	20	4428	4474	4531
Crooked Pond	142	1	UCIAMS-111582	Charcoal	4245	20	4733	4835	4849

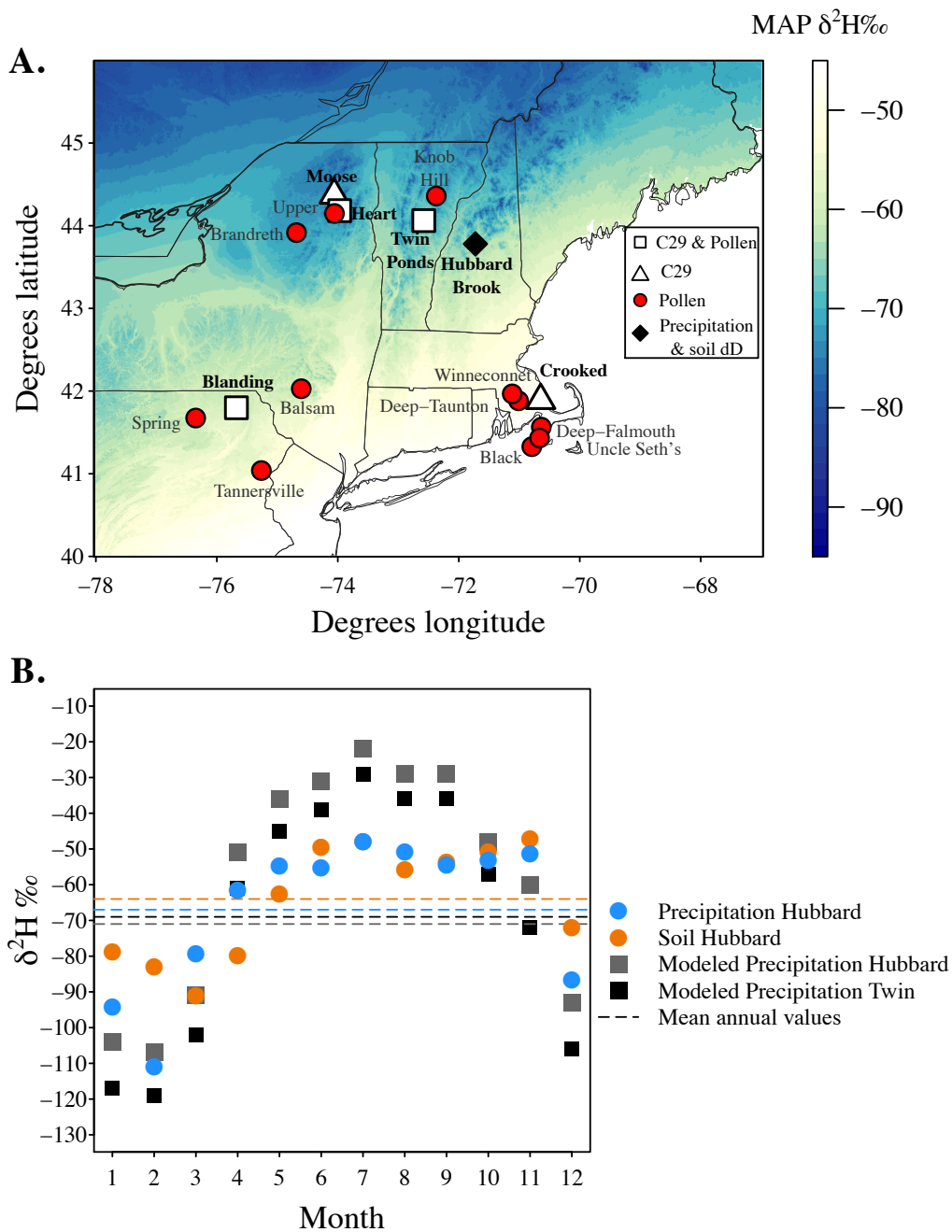
Crooked Pond	152	1	UCIAMS-111583	Charcoal	4635	25	5317	5412	5447
Crooked Pond	176	1	UCIAMS-111584	Charcoal	4840	25	5488	5581	5596
Crooked Pond	181	1	UCIAMS-111585	Charcoal	4915	20	5597	5634	5691
Crooked Pond	205	1	UCIAMS-83276	Charcoal	4715	20	5333	5382	5554
Crooked Pond	350**	5	Beta- 94238	Bulk	6860	60	7605	7694	7817
Crooked Pond	624**	8	Beta- 94239	Bulk	9220	70	10258	10387	10549

689 Notes:

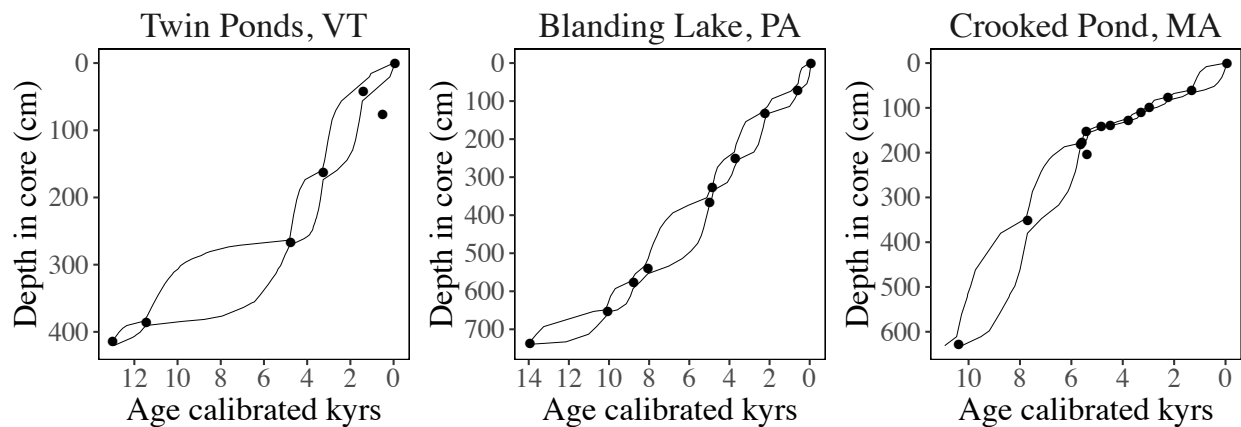
690 * Age reversal (not used in chronology)

691 ** Twin Ponds: age from Core TP48 (Mandl et al., 2016); Crooked Pond age from Core D

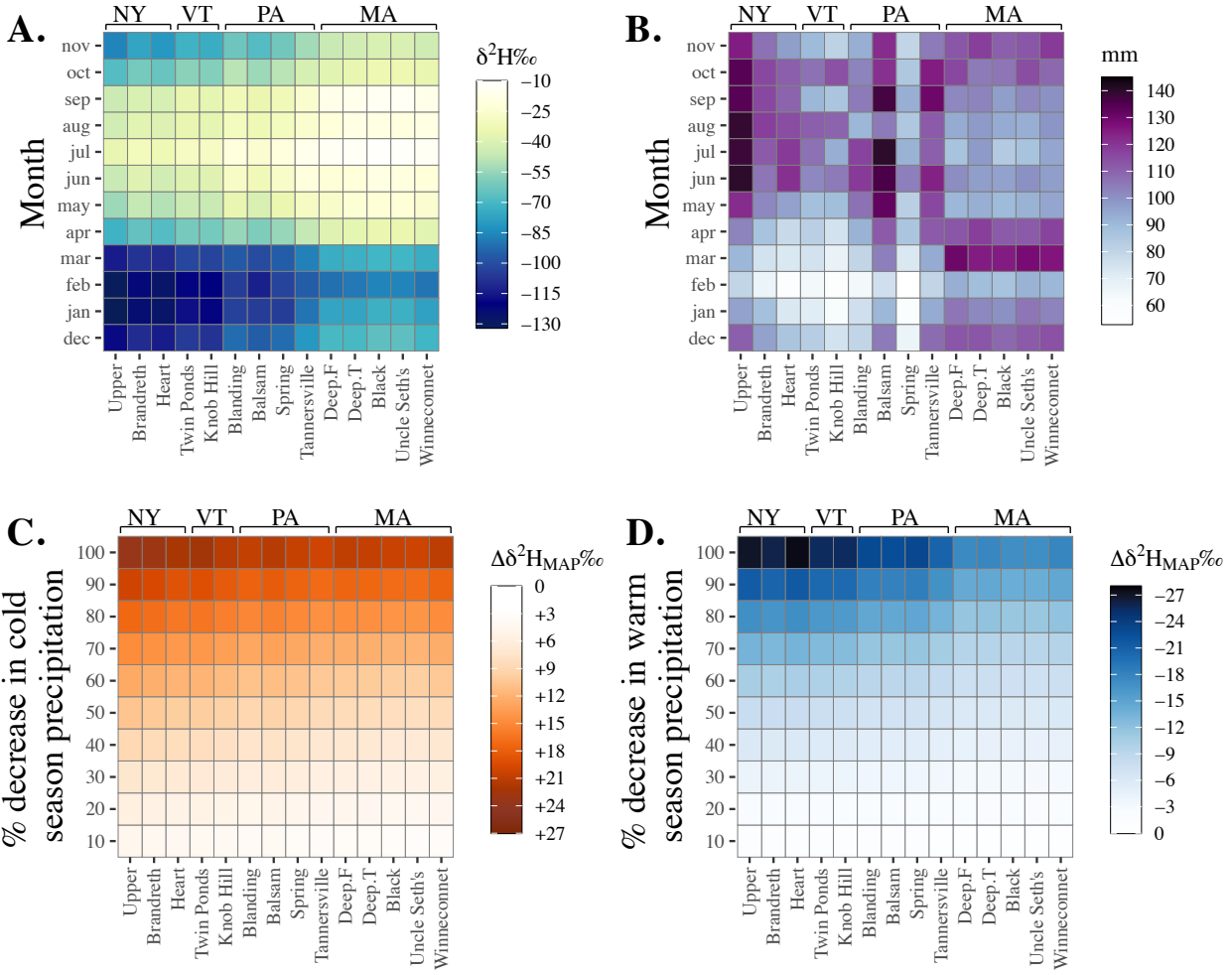
692 (Shuman et al., 2001)



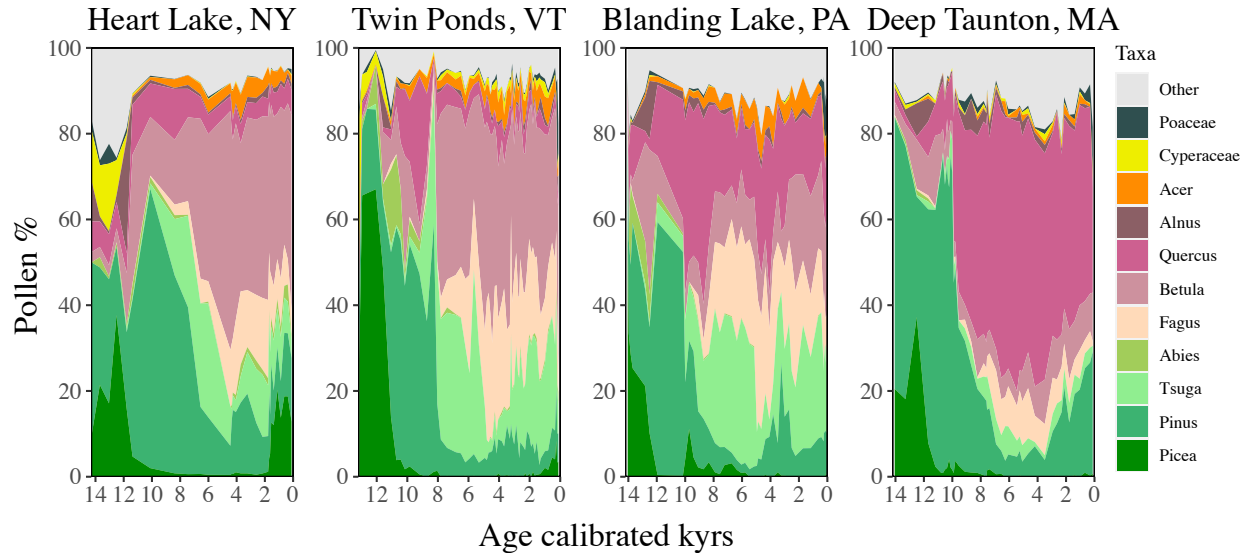
693 **Figure 1. A.** Map showing the northeastern U.S. region and the site locations for fossil pollen
 694 and *n*-C₂₉-alkane records; modeled mean annual precipitation $\delta^2\text{H}$ values ($\delta^2\text{H}_{\text{MAP}}$) are shown in
 695 the background with color scale on the right. **B.** Averaged monthly and annual $\delta^2\text{H}$ values of
 696 measured precipitation and soil moisture from Hubbard Brook, New Hampshire (Campbell and
 697 Greene, 2019; data collection 2006-2010) and modeled monthly and annual precipitation $\delta^2\text{H}$
 698 values (Bowen, G. J., 2020) at Hubbard Brook and Twin Ponds, Vermont.



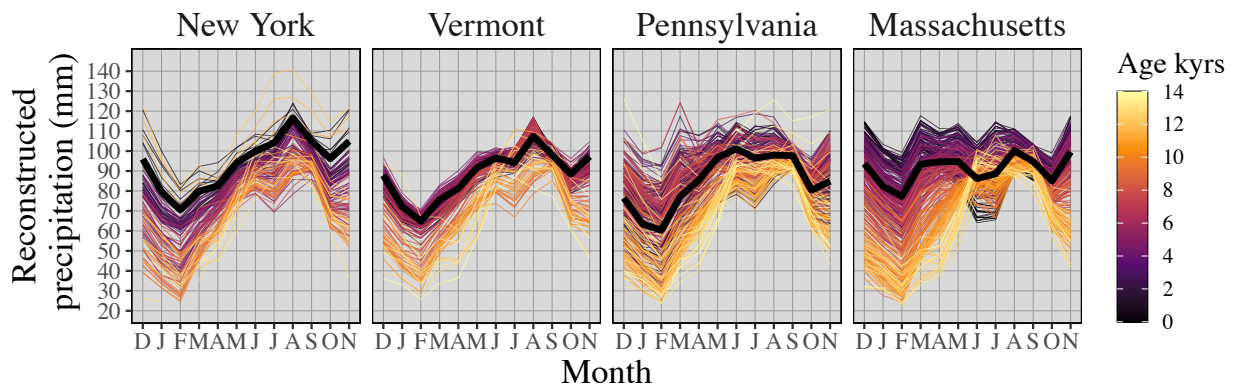
699 **Figure 2.** Age models for Twin Ponds (VT) (shallow water core), Blanding Lake (PA), and
700 Crooked Pond (MA). Radiocarbon ages are shown with black circles and the black lines
701 represent the 90th percent credible intervals of modeled ages.



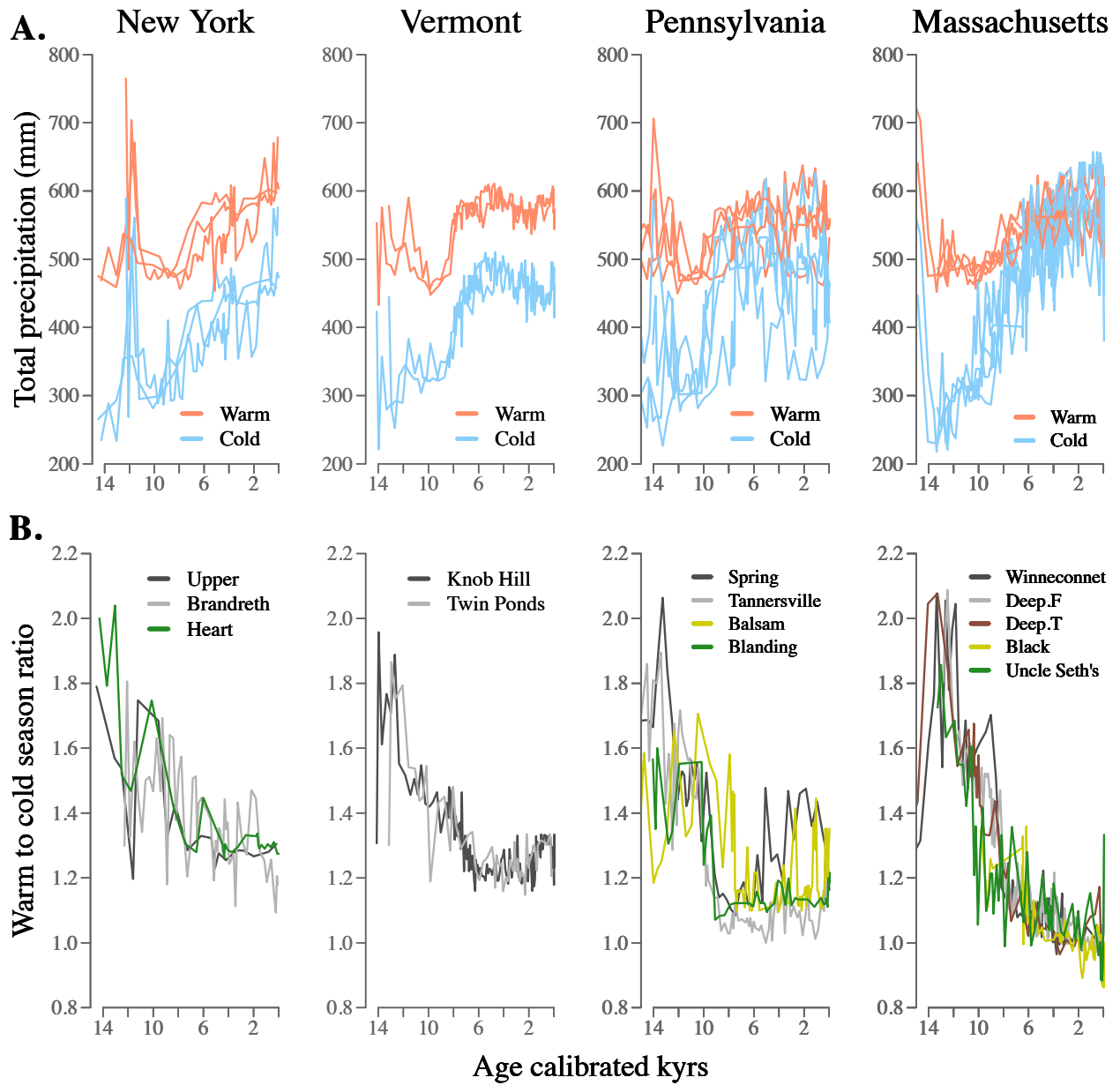
702 **Figure 3. A.** Monthly precipitation $\delta^2\text{H}$ values at individual sites (data from OIPC); **B.** Monthly
 703 precipitation input values at individual sites (data from Prism); **C.** Modeled change in $\delta^2\text{H}_{\text{MAP}}$
 704 values as a function of % decrease in cold season precipitation at individual sites; **D.** Modeled
 705 change in $\delta^2\text{H}_{\text{MAP}}$ values as a function of % decrease in warm season precipitation at individual
 706 sites.



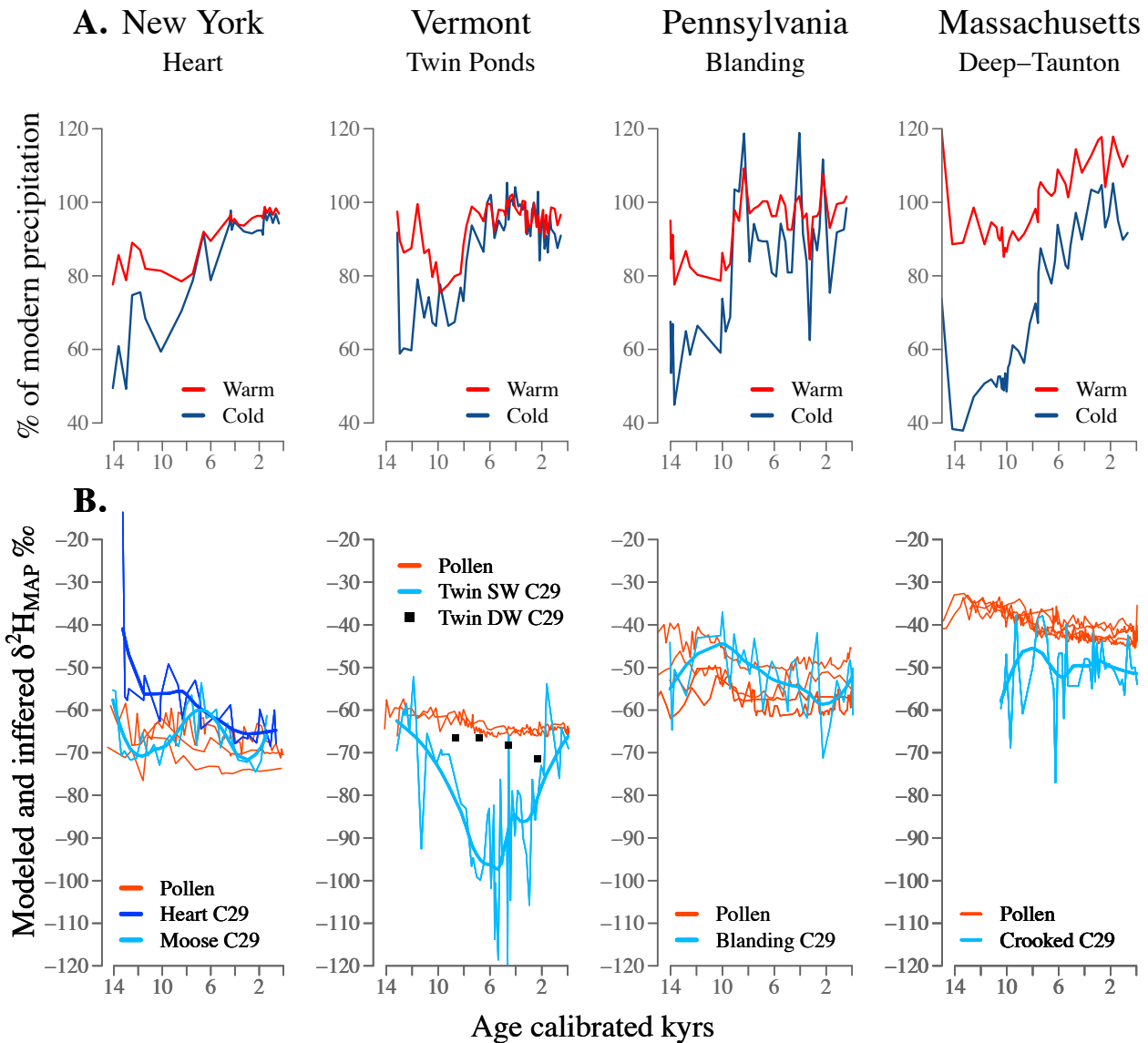
707 **Figure 4.** Changes in pollen percentages of major taxa (i.e., taxa with >5% abundance in at least
 708 5% of data) vs. age at Heart Lake, Blanding Lake, Twin Ponds (deep-water core) and at the
 709 nearby Deep-Taunton Pond (closest to Crooked Pond, MA). Gymnosperm taxa are shown in
 710 green, angiosperm taxa are shown with marron, orange, yellow, and dark green. “Other” includes
 711 all minor terrestrial pollen taxa (<5% abundance in 95% of data) from a list of 54 regional types
 712 used in the modern analog technique (Marsicek et al., 2013).



713 **Figure 5.** Pollen-inferred monthly precipitation values across individual regions (i.e., states) with
 714 calibrated age for color-scale. Each panel includes all the pollen-records from individual regions.
 715 Black lines represent monthly precipitation values for the core tops (i.e., modern) averaged
 716 across sites in each region.



717 **Figure 6. A.** Pollen-inferred seasonal precipitation inputs: warm season shown in orange, cold
 718 season shown in blue. Each panel includes all the pollen records from individual regions. **B.**
 719 Warm to cold season ratio of precipitation plotted for individual pollen records as well as
 720 regionally.



721 **Figure 7. A.** Pollen-inferred % of modern seasonal precipitation for selected sites; the last 600
 722 years are excluded to avoid European land clearance effects on the reconstructions. **B.** Modeled
 723 δ^2H_{MAP} values at all fossil pollen sites based on pollen inferred seasonal changes in precipitation
 724 (orange lines) and reconstructed δ^2H_{MAP} values based on the n -C₂₉-alkane (blue lines).
 725 Reconstructed δ^2H_{MAP} values at Twin Ponds from the sediment core collected in the shallow,
 726 near-shore region of the lake (0.79 m depth) are shown in blue and labeled “Twin SW C29”,
 727 while the reconstructed δ^2H_{MAP} values from the sediment core collected from the deepest
 728 location within the lake (7.8 m) are shown with black squares and labeled “Twin DW C29”.